Research Square

Preprints are preliminary reports that have not undergone peer review.
They should not be considered conclusive, used to inform clinical practice,
or referenced by the media as validated information.

Chiral-angle-selected spin splitting and spin-polarized conduction in nanotubes rolled from d-wave altermagnets

Ersoy Şaşıoğlu
ersoy.sasioglu@physik.uni-halle.de

Martin Luther University Halle-Wittenberg

Tom G. Saunderson
Martin Luther University Halle-Wittenberg

Börge Göbel
Martin Luther University Halle-Wittenberg

Ingrid Mertig
Martin Luther University Halle-Wittenberg

Samir Lounis
Martin Luther University Halle-Wittenberg

Article

Keywords:

Posted Date: November 9th, 2026

DOI: https://doi.org/10.21203/rs.3.rs-11406326/v1

License: This work is licensed under a Creative Commons Attribution 4.0 International License.
Read Full License

Additional Declarations: No competing interests reported.

Chiral-angle-selected spin splitting and spin-polarized conduction in nanotubes rolled from d-wave altermagnets

Ersoy Şaşıoğlu[1],* Tom G. Saunderson[1], Börge Göbel[1], Ingrid Mertig[1], and Samir Lounis[1]
[1] *Institute of Physics and Halle-Berlin-Regensburg Cluster of Excellence CCE, Martin Luther University Halle-Wittenberg, 06120 Halle (Saale), Germany*

Altermagnets combine compensated collinear magnetic order with momentum-dependent spin splitting, promising spin-polarized currents without stray fields. In two-dimensional (2D) d-wave altermagnets, however, this splitting changes sign between orthogonal directions and vanishes along nodal ones, so the spin polarization of a current depends on its direction relative to the crystal axes, and exploiting it requires currents aligned with specific crystallographic directions. Here we show that rolling a d-wave altermagnet into a nanotube fixes this direction structurally: although rolling removes the parent $C_4\mathcal{T}$ symmetry, the inherited splitting survives through zone folding as a selection rule set by the chiral angle. Tight-binding, symmetry, and first-principles analyses of symmetric and Janus nanotubes show that antinodal nanotubes are spin split, whereas the nodal nanotube remains exactly spin degenerate owing to a surviving mirror symmetry combined with spin reversal. In V_2O nanotubes, the ballistic transmission polarization decreases from 39% for the antinodal nanotube to zero for the nodal one at comparable total transmission. Our results identify nanotubes rolled from altermagnets as geometry-selected spin channels for nanoscale spintronics.

Altermagnets combine compensated collinear magnetic order with momentum-dependent spin splitting whose sign alternates between symmetry-related regions of the Brillouin zone [1–6]. Depending on crystal symmetry, the momentum dependence of the spin splitting can exhibit d-, g-, or higher-order wave symmetries [7, 8]. Experimental signatures of altermagnetic spin splitting have been reported in MnTe, CrSb, and KV_2Se_2O [9–11]. The coexistence of momentum-dependent spin splitting with compensated magnetic order makes altermagnets attractive for spintronics, offering spin-polarized electronic responses without requiring a net magnetization [12–14]. Low-dimensional systems are particularly appealing in this context because reduced dimensionality and structural transformations can modify the crystalline symmetries that govern altermagnetic spin splitting. A growing family of two-dimensional (2D) altermagnets has been predicted [15–24]. Among these systems, 2D d-wave altermagnets are particularly relevant because their spin splitting exhibits symmetry-defined nodal and antinodal directions. This anisotropy, however, also limits how the spin splitting can be exploited in a flat layer. The spin polarization of a longitudinal current depends on its direction relative to the crystal axes: it is finite for currents along antinodal directions and vanishes along nodal ones [12]. Using it therefore requires devices whose current direction is aligned with specific crystallographic axes, and any misalignment reduces the polarization. Cutting the layer into nanoribbons fixes the current direction, but introduces edges that could break the sublattice symmetries of the parent layer and could host edge states. This raises the question of how the characteristic spin splitting evolves when a parent 2D d-wave altermagnet is transformed into a one-dimensional structure without edges, and whether the resulting electronic states can support spin-polarized transport whose polarization is fixed by the structure itself.

In square-lattice 2D d-wave altermagnets, the opposite-spin magnetic sublattices are related by $C_4\mathcal{T}$ symmetry, which constrains the spin splitting to change sign between two orthogonal antinodal directions, with spin-degenerate nodal lines separating them. When a structural transformation removes this $C_4\mathcal{T}$ relation, the symmetry classification of the parent 2D altermagnet no longer directly applies. It is therefore not evident whether the parent d-wave spin splitting must disappear together with $C_4\mathcal{T}$, or whether its characteristic momentum dependence can remain encoded in the electronic structure of the resulting lower-dimensional system. Resolving this question is important for understanding how altermagnetic spin splitting evolves when both dimensionality and the symmetry of the parent system are altered.

Nanotubes provide a natural setting for addressing this problem. Rolling a 2D layer imposes periodic boundary conditions around the circumference, quantizing the circumferential momentum and converting the 2D electronic structure into one-dimensional (1D) subbands dispersing along the tube axis. In carbon nanotubes, the wrapping geometry selects the allowed momentum-space cuts and thereby determines whether a nanotube is metallic or semiconducting [25, 26]. Nanotubes and scrolls have also been realized from transition-metal dichalcogenides and Janus layers [27–32]. For a 2D d-wave altermagnet, this construction directly connects the wrapping geometry to the momentum-dependent spin splitting: the chiral angle, defined by the tube axis relative to an antinodal direction of the parent 2D layer, determines how the quantized momentum-space cuts sample its nodal and antinodal directions. Unlike a flat layer or a nanoribbon, a seamless nanotube fixes the transport direction relative to the parent lattice through its

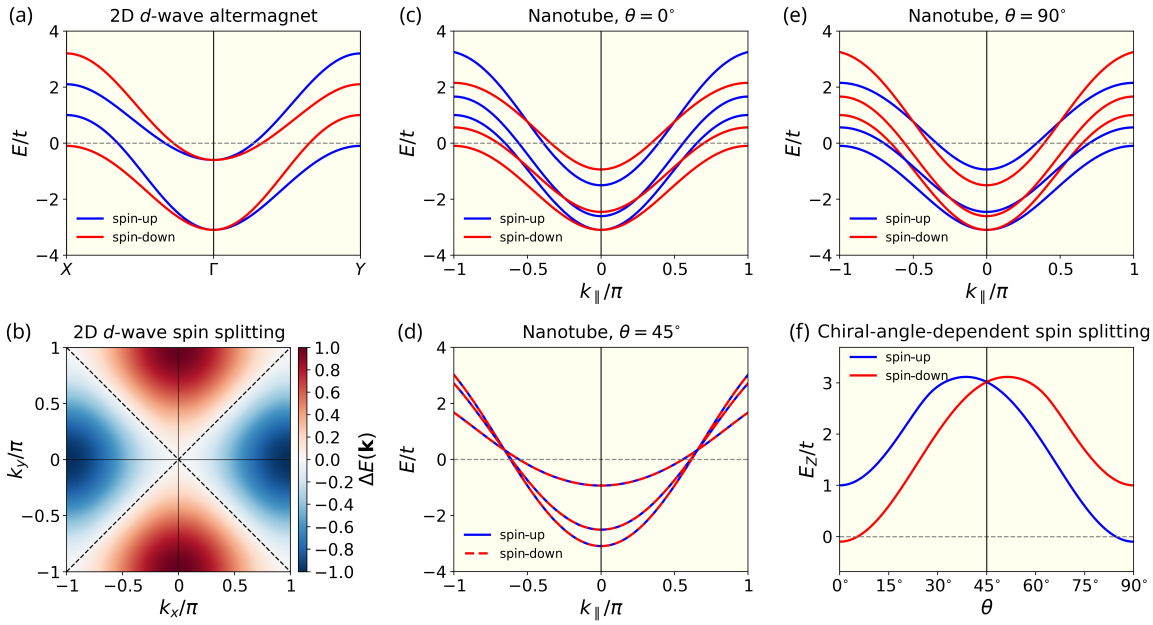


FIG. 1. **Zone folding of d-wave spin splitting into one-dimensional nanotube states**. (a) Band structure of the parent 2D d-wave altermagnet along X–Γ–Y. (b) Momentum-resolved spin splitting $\Delta E(\mathbf{k})$ of the parent system, showing antinodal regions with opposite signs of the spin splitting separated by symmetry-protected nodal lines. (c)–(e) Spin-resolved 1D band structures of nanotubes with chiral angles $\theta = 0°$, $45°$, and $90°$, respectively. These three high-symmetry nanotubes are achiral. The antinodal nanotubes at $\theta = 0°$ and $90°$ exhibit finite spin splitting with opposite signs for a given Néel vector, whereas the complete spectrum of the nodal nanotube at $\theta = 45°$ is spin degenerate. (f) Spin-resolved energies of the $k_\perp = 0$ subband at the 1D zone-boundary point Z as a function of chiral angle θ. The splitting evolves continuously between the two antinodal limits, vanishes at the nodal limit, and reverses sign. For small $k_\parallel$, Eq. (4) predicts a $\cos(2\theta)$ dependence. At Z, the angular dependence deviates from this form because the spin splitting is no longer linear in the d-wave form factor.

wrapping geometry and has no edges. At the same time, rolling makes the axial and circumferential directions inequivalent and therefore removes the parent $C_4\mathcal{T}$ symmetry irrespective of the chiral angle. The nanotube geometry thus combines chiral-angle-dependent zone folding of the parent d-wave electronic structure with the loss of the symmetry that defines the parent altermagnetic state.

Here, we show that nanotubes rolled from 2D d-wave altermagnets exhibit a chiral-angle-selected spin splitting inherited from the parent d-wave electronic structure despite the loss of $C_4\mathcal{T}$ symmetry. A minimal tight-binding model and symmetry analysis establish the selection rule: nanotubes whose axes are aligned with an antinodal direction are spin split, the two antinodal orientations being related by the parent $C_4\mathcal{T}$ operation with the sublattices interchanged, whereas the nodal nanotube remains exactly spin degenerate and magnetically compensated owing to a surviving mirror symmetry combined with spin reversal. First-principles calculations for V_2O and three additional compounds, including two Janus systems, demonstrate that this behavior persists despite structural changes induced by rolling and, in the antinodal nanotubes, sublattice moment imbalance. Comparison with the zone-folded electronic structure of the parent 2D layer further shows that the chiral-angle dependence of the spin splitting originates from the parent d-wave electronic structure rather than from curvature itself. Spin-resolved transport calculations reveal the corresponding conduction signature: across the calculated chiral angles, the transmission polarization decreases from 39% for the antinodal nanotube to zero for the nodal nanotube, while the total transmission remains comparable. Because the wrapping geometry fixes the current direction, nanotubes rolled from the same magnetic monolayer thus act as spin-polarizing or spin-neutral conductors depending only on their chiral angle. These results establish the chiral angle as a structural parameter that selects both spin splitting and spin-polarized conduction in nanotubes rolled from 2D d-wave altermagnets.

RESULTS

Zone folding of d-wave spin splitting

To separate geometrical and symmetry principles from material-specific effects, we first consider a minimal two-sublattice tight-binding model of a metallic d-wave altermagnet on a square lattice. Model parameters are given in the Supplementary Information. The Bloch Hamilto-

nian is

$$H_\sigma(\mathbf{k}) = \varepsilon(\mathbf{k})\tau_0 + t_{AB}(\mathbf{k})\tau_x + [J\sigma + \lambda g_d(\mathbf{k})]\,\tau_z, \quad (1)$$

where $\sigma = \pm 1$ is the spin index, τ_i are Pauli matrices in sublattice space, $\varepsilon(\mathbf{k})$ is the spin-independent dispersion, $t_{AB}(\mathbf{k})$ the intersublattice hopping, J the staggered exchange field, and λ the strength of the d-wave term with form factor

$$g_d(\mathbf{k}) = \cos k_x - \cos k_y. \quad (2)$$

The resulting spin splitting has two orthogonal antinodal directions with opposite signs, separated by nodal lines $k_x = \pm k_y$ along which the bands are spin degenerate [Figs. 1(a) and 1(b)].

Rolling the layer quantizes the circumferential momentum. We define the chiral angle θ as the angle between the nanotube axis and an antinodal direction of the parent layer, and introduce momenta $k_\parallel$ along and $k_\perp$ around the tube. The circumferential component is quantized, $k_\perp = 2\pi n/C$ for circumference C and integer n, while $k_\parallel$ remains continuous, as in the standard nanotube zone-folding construction [25, 26]. Expanding Eq. (2) around Γ in the rotated coordinates gives

$$g_d \propto \cos(2\theta)(k_\parallel^2 - k_\perp^2) - 2\sin(2\theta)k_\parallel k_\perp. \quad (3)$$

For the $n = 0$ subband ($k_\perp = 0$), the spin splitting therefore scales as

$$\Delta_{\mathrm{tube}}(\theta) \propto \cos(2\theta)\, k_\parallel^2, \quad (4)$$

for small $k_\parallel$, where the splitting is proportional to λg_d. It is largest in magnitude at $\theta = 0°$ and $90°$, vanishes at $\theta = 45°$, and reverses sign between the two antinodal directions. At larger $k_\parallel$, the same qualitative behavior persists, but the angular dependence departs from $\cos(2\theta)$ because the spin splitting is no longer linear in the d-wave form factor [Fig. 1(f)]. For $n \neq 0$, finite-$k_\perp$ terms in Eq. (3) contribute, and no universal $\cos(2\theta)$ dependence is expected.

The band structures for $\theta = 0°$, $45°$, and $90°$ are shown in Figs. 1(c)–1(e). The two antinodal nanotubes are spin split with opposite signs, whereas the nodal nanotube is spin degenerate. The sign reversal between $\theta = 0°$ and $90°$ is required by symmetry: the parent $C_4\mathcal{T}$ symmetry operation maps the nanotube rolled along [10] onto that rolled along [01] with the two sublattices interchanged, so the two nanotubes have identical spectra with the spin labels reversed. The sign of the splitting is therefore defined relative to the Néel vector: reversing the Néel vector of the $\theta = 0°$ nanotube yields the spectrum of the $\theta = 90°$ nanotube. The physically distinct cases selected by the chiral angle are thus spin-split (antinodal) and spin-degenerate (nodal) nanotubes. The limiting cases are therefore the antinodal and nodal nanotubes, with chiral nanotubes at intermediate chiral angles [Fig. 1(f)].

Zone folding also maps states from finite momenta of the parent Brillouin zone onto the reduced 1D zone. Spin-split states can therefore appear at the nanotube zone center even though the parent Γ point is spin degenerate by symmetry. This provides a way to distinguish effects already present through zone folding from those introduced by curvature, by comparing the nanotube bands with those of corresponding unrolled rectangular supercells, as we do below.

Symmetry of the rolled structures

Rolling makes the axial and circumferential directions inequivalent for every chiral angle. Consequently, the $C_4\mathcal{T}$ symmetry that relates the two sublattices of the parent 2D layer does not survive rolling. The nanotubes should therefore not, in general, be classified as altermagnets in the same symmetry sense as the parent layer. Whether spin degeneracy is retained after rolling is instead determined by the symmetries that remain in the nanotube.

For the nodal nanotube ($\theta = 45°$), the axis lies along a diagonal of the parent lattice. In the parent layer, a diagonal mirror exchanges the two opposite-spin sublattices and therefore enters the spin group in combination with spin reversal. After rolling, this mirror becomes a vertical mirror plane containing the nanotube axis. Because this mirror plane also contains the radial direction, the inequivalence of the inner and outer sides of the nanotube does not break the mirror symmetry. The same remains true for the out-of-plane structural asymmetry of a Janus layer. The combined operation leaves $k_\parallel$ unchanged, reverses the circumferential angular momentum $n \to -n$, and reverses spin. It therefore pairs $(n, \uparrow)$ with $(-n, \downarrow)$ at every $k_\parallel$. Thus, an individual $n \neq 0$ subband need not be spin degenerate. Nevertheless, the complete spectrum is spin degenerate at each $k_\parallel$, since $E_{n\uparrow}(k_\parallel) = E_{-n\downarrow}(k_\parallel)$. The same symmetry keeps the two magnetic sublattices equivalent, so the nodal nanotube is magnetically compensated. Since the nanotube has no edges, this protection holds for the entire conductor, whereas in a nanoribbon cut along the nodal direction the edges could break the sublattice-exchanging mirror.

For the antinodal nanotube ($\theta = 0°$), the corresponding vertical mirror maps each sublattice onto itself and does not involve spin reversal. Thus, unlike in the nodal nanotube, no surviving symmetry exchanges the two sublattices. Their local environments become inequivalent after rolling: the anisotropic bonds of one sublattice lie along the tube axis, whereas those of the other lie around the circumference. Consequently, spin splitting is symmetry allowed, and the two sublattices are not required to have equal magnetic moments. Generic chiral nanotubes likewise allow spin splitting because they lack the corresponding vertical mirror symmetry. These symme-

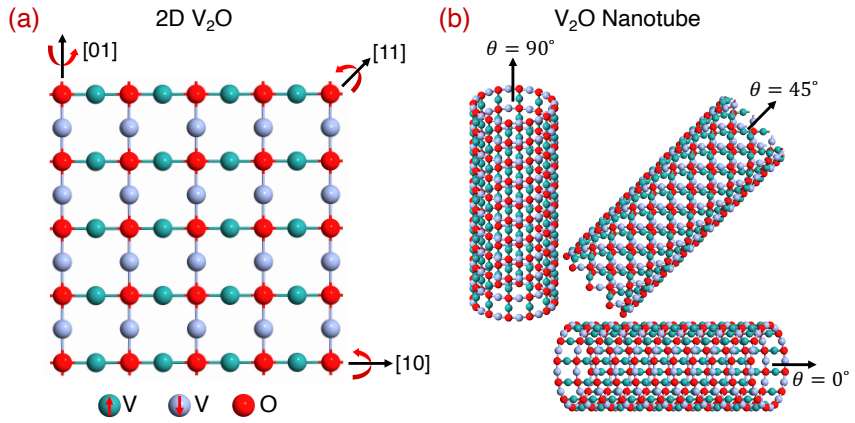


FIG. 2. **Atomistic realization of nanotubes rolled from a 2D d-wave altermagnet**. (a) Checkerboard 2D V_2O with opposite-spin V sublattices and high-symmetry crystallographic directions [10], [11], and [01]. (b) Representative achiral V_2O nanotubes with chiral angles $\theta = 0°$, 45°, and 90°, defined by the orientation of the nanotube axis relative to an antinodal direction of the parent layer. The $\theta = 0°$ and 90° nanotubes are antinodal, whereas the $\theta = 45°$ nanotube is nodal.

try arguments explain why spin degeneracy and magnetic compensation are protected in the nodal nanotube but not in the antinodal nanotubes considered below.

First-principles realization in V_2O nanotubes

We next test the model and symmetry predictions using checkerboard V_2O as a minimal first-principles realization. Its square-lattice magnetic structure exhibits the $d_{x^2-y^2}$ spin splitting of the model. Figure 2(a) shows the parent layer with the antinodal [10] and [01] directions and the nodal [11] direction, while Fig. 2(b) shows the corresponding achiral nanotubes with $\theta = 0°$, 45°, and 90°. The parent band structure [Fig. 3(a)] exhibits spin splitting that reverses sign between X–Γ and Γ–Y and vanishes at Γ, consistent with the $d_{x^2-y^2}$ pattern of the model.

To separate zone folding from curvature, we compare the nanotube electronic structure with that of the corresponding unrolled rectangular supercell. For the $\theta = 0°$ nanotube, this is a 1×18 supercell whose Γ–X direction becomes the nanotube axis [Fig. 3(b)]. Its folded bands already show spin-split states at the supercell zone center. The nanotube bands for $\theta = 0°$, 45°, and 90° [Figs. 3(c)–3(e)] reproduce the selection rule of the model: the two antinodal nanotubes are spin split with opposite signs along Γ–Z, whereas the complete spectrum of the nodal nanotube is spin degenerate. The close correspondence between the $\theta = 0°$ nanotube and the unrolled supercell (see also Fig. S1 of the Supplementary Information) shows that the spin splitting is already encoded in the zone-folded electronic structure of the parent 2D layer. Curvature and structural relaxation modify the bands quantitatively but are not required for the characteristic spin splitting.

The V_2O nanotubes remain nearly magnetically compensated after rolling. For the $\theta = 0°$ nanotube with $R = 11.04$ Å, the two V sublattices carry $+2.63\ \mu_B$ and $-2.61\ \mu_B$, corresponding to a residual magnetic moment $\Delta M = |M_1 + M_2| \simeq 0.02\ \mu_B$, with negligible O moments. As discussed above, such a sublattice moment imbalance is symmetry allowed for the antinodal nanotube, where no symmetry operation relates the two sublattices.

Chiral-angle-selected spin-polarized transmission

A spin-split band structure does not by itself determine the spin polarization of a current, which is governed by the propagating states at a given energy. We therefore calculate the spin-resolved ballistic transmission $T_\sigma(E)$ along the axes of periodic V_2O nanotubes with $\theta = 0°$, $\simeq 18°$, $\simeq 27°$, and 45°. Here, $T_\sigma(E)$ counts the propagating spin-σ modes at energy E. The intermediate-angle nanotubes are chiral and track the evolution between the antinodal and nodal limits.

For the antinodal $\theta = 0°$ nanotube [Fig. 4(a)], the spin channels are strongly imbalanced at the Fermi level, with $T_\uparrow(E_F) = 52$ and $T_\downarrow(E_F) = 23$ ($T = 75$). For $\theta \simeq 18°$ and $\simeq 27°$, the corresponding values are $(46, 28)$ and $(42, 28)$, with $T = 74$ and 70 [Figs. 4(b) and 4(c)]. For the nodal $\theta = 45°$ nanotube, $T_\uparrow(E_F) = T_\downarrow(E_F) = 35$ ($T = 70$) [Fig. 4(d)]. Defining the transmission polarization as

$$P_T(E) = \frac{T_\uparrow(E) - T_\downarrow(E)}{T_\uparrow(E) + T_\downarrow(E)}, \tag{5}$$

we find that $P_T(E_F)$ decreases from 38.7% at $\theta = 0°$ to 24.3% and 20.0% for the two chiral nanotubes and vanishes at $\theta = 45°$, while the total transmission changes by less than 10%. For the nodal nanotube, the mirror operation discussed above pairs each spin-up propagating mode with a spin-down propagating mode at the same

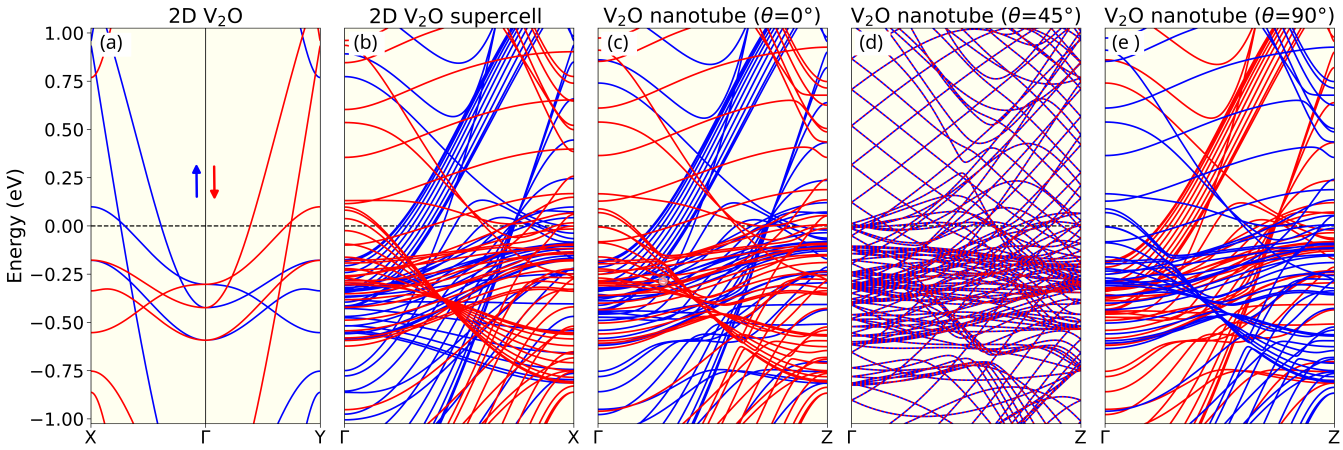


FIG. 3. **Zone folding and spin splitting in V_2O nanotubes**. (a) Spin-resolved band structure of primitive-cell 2D V_2O along X–Γ–Y. (b) Band structure of a 1×18 unrolled rectangular V_2O supercell along Γ–X, showing the folded electronic structure prior to rolling. (c)–(e) Spin-resolved band structures of the achiral V_2O nanotubes with chiral angles $\theta = 0°$, $45°$, and $90°$, respectively, calculated along the nanotube axis (Γ–Z). The two antinodal nanotubes exhibit finite spin splitting with opposite signs for a given Néel vector, consistent with the parent $C_4\mathcal{T}$ symmetry relation between the [10] and [01] directions, whereas the complete spectrum of the nodal nanotube remains spin degenerate.

energy, so $T_\uparrow(E) = T_\downarrow(E)$ holds at all energies, not only at the Fermi level.

The transmission polarization does not follow the $\cos(2\theta)$ dependence of the $n = 0$ subband because $T_\sigma(E)$ collects contributions from many subbands with different dispersions. Moreover, commensurate nanotubes with different chiral angles differ slightly in radius and unit cell, so the small variation of the total transmission cannot be attributed uniquely to θ. Across the calculated chiral angles, the spin-channel imbalance decreases from $T_\uparrow - T_\downarrow = 29$ at $\theta = 0°$ to zero at $\theta = 45°$, while the total transmission remains comparable. In the parent 2D layer, the antinodal and nodal directions are already distinguished by spin-polarized and spin-unpolarized longitudinal conduction, respectively [12]. There, however, this distinction must be imposed by the device geometry, by aligning the current with a crystallographic direction. In a nanotube, the current direction relative to the parent lattice is fixed by the wrapping geometry, so the chiral angle selects the spin polarization of the conducting channels, which thus becomes a property of the structure rather than of the device layout.

To illustrate the corresponding current response, Figs. 4(e)–4(h) show the spectral currents

$$I_\sigma(E) = \frac{e}{h} T_\sigma(E)\,[f_R(E) - f_L(E)]\,, \tag{6}$$

evaluated with electrochemical potentials $E_{F,L} = -0.2$ eV and $E_{F,R} = +0.2$ eV relative to the equilibrium Fermi level, corresponding to an electrochemical-potential difference of 0.4 eV, while the zero-bias transmission is held fixed. The charge spectral current $I_{\rm ch} = I_\uparrow + I_\downarrow$ remains comparable across the calculated chiral angles, whereas the spin-channel spectral current $I_{\rm sp} = I_\uparrow - I_\downarrow$ decreases toward the nodal limit and vanishes at $\theta = 45°$. Because the transmission is not recalculated self-consistently at finite bias, these spectral currents represent a fixed zero-bias transmission approximation rather than a self-consistent finite-bias transport calculation.

Robustness across material realizations

To test whether the selection rule extends beyond V_2O, we consider three additional material realizations with different chemical and structural environments: V_2OSe_2, a symmetric monolayer; V_2OSeTe, a Janus monolayer with out-of-plane structural asymmetry; and Fe_2SSe, a Janus monolayer that develops a substantially larger sublattice moment imbalance upon rolling. The V_2X_2O family is closely related to the experimentally realized layered altermagnets KV_2Se_2O and RbV_2Te_2O [11, 33, 34]. Further candidate parent monolayers identified in recent computational searches [35, 36] are listed in Table S1 of the Supplementary Information. These materials define a broader candidate space but are not considered here as validated nanotube realizations.

Rolling introduces an inequivalence between the inner and outer sides of a nanotube and can modify local bonding, hybridization, and magnetic moments. To examine how these effects depend on tube radius, we considered $\theta = 0°$ nanotubes with radii of approximately 5, 10, and 15 Å for each material (Table S2 of the Supplementary Information). For V_2OSe_2, the residual magnetic moment $\Delta M = |M_1 + M_2|$ decreases from 0.15 to 0.04 and 0.02 μ_B with increasing radius. The Janus V_2OSeTe nanotubes show larger values of 0.35, 0.15, and 0.10 μ_B, whereas Fe_2SSe reaches 0.69 μ_B at the smallest radius and decreases to 0.42 and 0.26 μ_B at the larger radii. The sys-

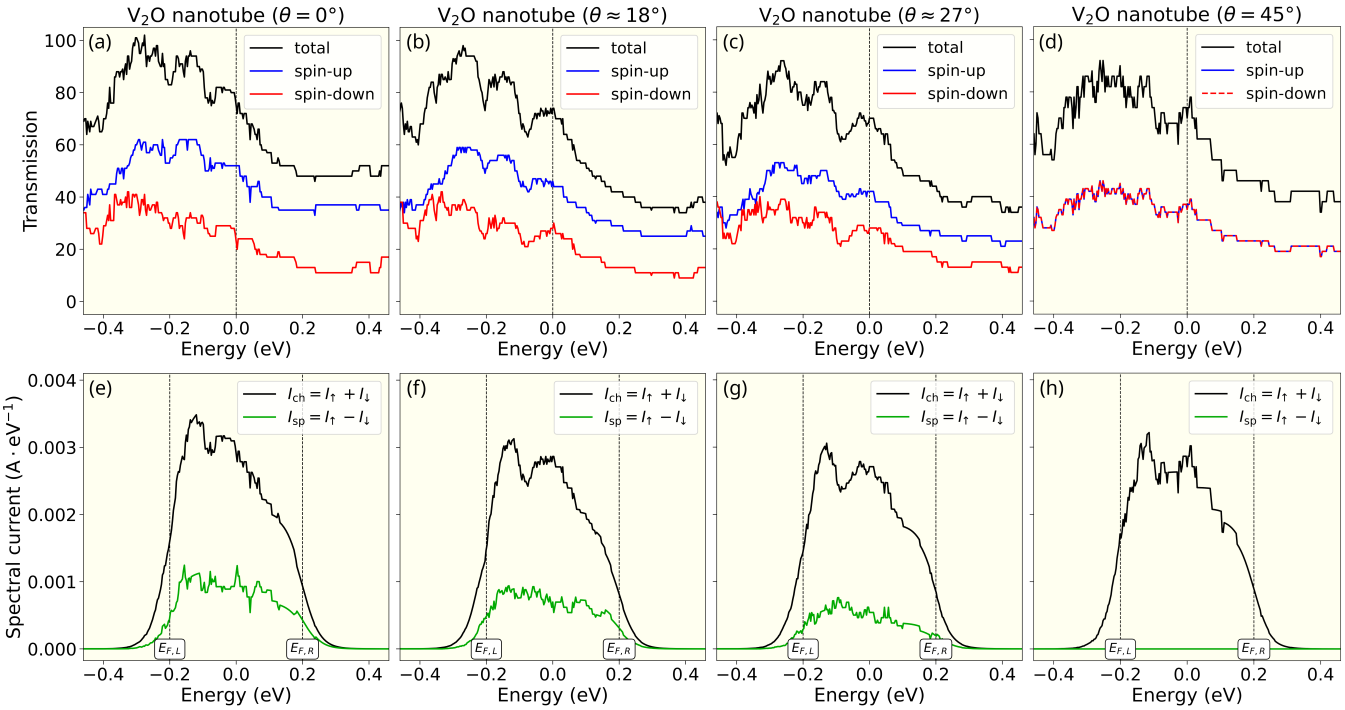


FIG. 4. **Chiral-angle-selected spin-polarized transmission in V_2O nanotubes**. (a)–(d) Zero-bias spin-resolved ballistic transmission spectra for nanotubes with chiral angles $\theta = 0°$, $\simeq 18°$, $\simeq 27°$, and $45°$, respectively. The $\theta = 0°$ and $45°$ nanotubes are achiral, whereas the intermediate-angle nanotubes are chiral. The total transmission and the spin-up and spin-down contributions are shown as functions of energy, with the equilibrium Fermi level set to zero. Across the calculated chiral angles, the transmission polarization decreases toward the nodal limit and vanishes for the $\theta = 45°$ nanotube, where $T_\uparrow(E) = T_\downarrow(E)$ at all energies by symmetry. (e)–(h) Energy-resolved spectral currents evaluated from the corresponding zero-bias transmission spectra with electrochemical potentials $E_{F,L} = -0.2$ eV and $E_{F,R} = +0.2$ eV relative to the equilibrium Fermi level, corresponding to a 0.4 eV electrochemical-potential difference. The charge and spin-channel spectral currents are defined as $I_{\rm ch} = I_\uparrow + I_\downarrow$ and $I_{\rm sp} = I_\uparrow - I_\downarrow$, respectively. The charge spectral current remains of comparable magnitude across the calculated chiral angles, whereas the spin-channel spectral current decreases toward the nodal limit and vanishes at $\theta = 45°$.

tematic reduction of ΔM with increasing radius is consistent with the weakening of curvature-induced inner–outer inequivalence.

Despite these material-dependent differences, the characteristic antinodal–nodal distinction remains robust (Fig. S2 of the Supplementary Information). For V_2OSeTe, the $\theta = 0°$ nanotube exhibits finite spin splitting and closely follows the zone-folded bands of the corresponding unrolled supercell, whereas the complete spectrum of the $\theta = 45°$ nanotube remains spin degenerate. Fe_2SSe exhibits larger quantitative deviations between the nanotube and unrolled-supercell bands, consistent with its stronger structural and magnetic response to rolling, but retains the same qualitative distinction between the antinodal and nodal nanotubes. These results are consistent with the symmetry analysis: structural changes induced by rolling, out-of-plane Janus asymmetry, and sublattice moment imbalance can modify the electronic structure and the magnitude of the spin splitting in the antinodal nanotubes, whereas the nodal spin degeneracy remains protected as long as the sublattice-exchanging mirror symmetry combined with spin reversal is preserved.

DISCUSSION

Our results separate two properties that coincide in the parent 2D altermagnet: the symmetry that defines the altermagnetic state and the momentum-dependent spin splitting it produces. Rolling removes the $C_4\mathcal{T}$ symmetry for every chiral angle, so the nanotubes are not altermagnets in the same symmetry-classification sense as their parent 2D layer. Nevertheless, the underlying magnetic order and exchange splitting persist after rolling, while zone folding carries the momentum dependence of the parent d-wave spin splitting into the 1D electronic structure. How this splitting appears in the nanotube spectrum is then selected by the chiral angle and constrained by the symmetries that remain after rolling. The antinodal nanotubes exhibit spin splitting, with opposite signs for the two antinodal orientations at a fixed Néel vector, while generic chiral nanotubes lack the corresponding vertical mirror symmetry and therefore allow spin

splitting. In contrast, the nodal nanotube remains spin degenerate because a sublattice-exchanging mirror combined with spin reversal survives rolling. The same symmetry keeps the two magnetic sublattices equivalent and therefore enforces magnetic compensation in the nodal nanotube, whereas no corresponding constraint exists for the antinodal nanotubes, allowing curvature-induced sublattice moment imbalance. Similar principles may apply to nanoscrolls, curved ribbons, and other quasi-1D structures formed from anisotropic magnetic layers, where structural transformations modify the symmetries and electronic structure inherited from the parent layer.

The transport results show that the inherited spin splitting is reflected in the propagating channels. Nanotubes rolled from the same magnetic monolayer can exhibit spin-polarized or spin-unpolarized ballistic conduction depending on their chiral angle, while retaining comparable total transmission. In particular, symmetry enforces equal transmission in the two spin channels for the nodal nanotube, whereas the calculated antinodal nanotube exhibits a transmission polarization of 38.7% at the Fermi level. These results demonstrate that the chiral angle can select the transmission polarization of nanotubes rolled from the same parent 2D altermagnet, while substantial transmission polarization can coexist with a small residual magnetic moment. This is the main practical difference from the parent layer. In a flat d-wave altermagnet, the spin polarization of the current is selected by the direction in which the current is driven, so it depends on the device layout and is reduced by any misalignment. In a nanotube, the wrapping geometry fixes the current direction relative to the parent lattice, the conductor has no edges, and the nodal case is protected by symmetry. Spin-polarized and spin-neutral conduction then become properties of the conductor itself, identifying nanotubes rolled from altermagnets as geometry-selected spin channels for nanoscale spintronics.

The implications for spintronic applications should be considered within the scope of the present calculations. The behavior demonstrated here is confirmed for several structurally distinct nanotube realizations, whereas the broader set of 2D altermagnets identified in the Supplementary Information should be regarded as a candidate space rather than as validated nanotube systems; the stability, magnetic configuration, and electronic structure of each rolled material must be established individually. Likewise, the transport calculations describe zero-bias ballistic transmission and spectral currents evaluated within a fixed zero-bias transmission approximation, rather than a self-consistent finite-bias transport calculation. Contacts, disorder, defects, finite-temperature effects, and scattering may modify the transmission polarization in realistic devices, and explicit device-level calculations will be required to assess potential spintronic functionalities.

Note added. After the original submission of this manuscript, we became aware of an independent work, posted around the same time, on spin-dependent phenomena in nanotubes rolled from two-dimensional altermagnets, including spin filtering and persistent spin currents [37]. Subsequently, a related preprint appeared on p-wave magnetism in chiral nanotubes [38].

METHODS

Tight-binding calculations

Nanotube states of the model in Eq. (1) were obtained by rotating the momentum coordinates according to the chiral angle θ and imposing periodic boundary conditions around the circumference. This quantizes the circumferential momentum $k_\perp$, while $k_\parallel$ remains continuous along the nanotube axis, yielding the 1D zone-folded subbands. Model parameters and further numerical details are provided in the Supplementary Information.

First-principles calculations

First-principles calculations were performed within density-functional theory using the generalized gradient approximation in the Perdew–Burke–Ernzerhof (PBE) parametrization, as implemented in QuantumATK, with norm-conserving PseudoDojo pseudopotentials and localized atomic-orbital basis sets [39–41]. All calculations were collinear and performed without spin–orbit coupling. Atomic structures were relaxed until the residual forces were below 0.01 eV/Å. A vacuum region of more than 20 Å was used to separate periodic images in the nonperiodic directions. Brillouin-zone sampling employed $20 \times 20 \times 1$ Monkhorst–Pack meshes for the monolayers and at least 20 k points along the periodic nanotube axis. Nanotubes were constructed from commensurate supercells of the parent monolayers for the corresponding chiral angles. Construction details and additional computational parameters are provided in the Supplementary Information.

Spin-resolved transmission

Spin-resolved ballistic transmission spectra were calculated with QuantumATK for periodic nanotubes, with transport along the nanotube axis and no separate scattering region. In this periodic geometry, $T_\sigma(E)$ counts the number of propagating spin-σ modes at energy E. All transmission spectra were calculated at zero bias. The spectral currents shown in Figs. 4(e)–4(h) were evaluated from Eq. (6) using the zero-bias transmission spectra and electrochemical potentials $E_{F,L} = -0.2$ eV and $E_{F,R} = +0.2$ eV relative to the equilibrium Fermi level,

corresponding to an electrochemical-potential difference of 0.4 eV. The transmission spectra were held fixed and were not recalculated self-consistently at finite bias.

DATA AVAILABILITY

The data supporting the findings of this study, including the numerical data underlying the electronic-structure and transport results, are available from the corresponding author upon reasonable request.

CODE AVAILABILITY

The first-principles and transport calculations were performed using the commercially available QuantumATK software. The tight-binding model and all parameters required to reproduce the calculations are provided in the Supplementary Information. The custom codes used to implement the tight-binding calculations are available from the corresponding author upon reasonable request.

ACKNOWLEDGEMENTS

This work was supported by the Deutsche Forschungsgemeinschaft (DFG) through CRC/TRR 227, Project No. B12 (Project ID 328545488), and Grants No. LO 1659/10-1, No. LO 1659/13-1, and No. SA 3174/1-1, and by the European Innovation Council (EIC) Pathfinder Open project, Grant No. 101129641. T.G.S. acknowledges computing time provided through the Gauss Centre for Supercomputing e.V. on the supercomputer JUWELS at Forschungszentrum Jülich under project superorb.

AUTHOR CONTRIBUTIONS

E.Ş. conceived the study and performed the first-principles and transport calculations. T.G.S. and B.G. performed the tight-binding calculations and contributed to the theoretical analysis. I.M. and S.L. supervised the project. All authors contributed substantially to the interpretation of the results. E.Ş. wrote the manuscript with input from all authors.

COMPETING INTERESTS

The authors declare no competing interests.

* ersoy.sasioglu@physik.uni-halle.de

[1] L.-D. Yuan, Z. Wang, J.-W. Luo, and A. Zunger, Prediction of low-z collinear and noncollinear antiferromagnetic compounds having momentum-dependent spin splitting even without spin-orbit coupling, Physical Review Materials **5**, 014409 (2021).
[2] L. Šmejkal, R. González-Hernández, T. Jungwirth, and J. Sinova, Crystal time-reversal symmetry breaking and spontaneous hall effect in collinear antiferromagnets, Science Advances **6**, eaaz8809 (2020).
[3] L. Šmejkal, J. Sinova, and T. Jungwirth, Beyond conventional ferromagnetism and antiferromagnetism: A phase with nonrelativistic spin and crystal rotation symmetry, Physical Review X **12**, 031042 (2022).
[4] L. Šmejkal, Y. Mokrousov, B. Yan, and A. H. MacDonald, Altermagnetism and spin-splitting by crystal symmetry, Nature Physics **18**, 242 (2022).
[5] L. Šmejkal, J. Sinova, and T. Jungwirth, Emerging research landscape of altermagnetism, Nature Reviews Materials **7**, 482 (2022).
[6] T. Jungwirth *et al.*, Altermagnetism, Nature Reviews Physics **6**, 560 (2024).
[7] I. I. Mazin, Altermagnetism in MnTe: Origin, predicted manifestations, and routes to detwinning, Physical Review B **107**, L100418 (2023).
[8] N. Giuli, N. Bittner, M. T. Mercaldo, M. Cuoco, P. Gentile, S. M. Winter, and R. Valentí, Interaction-driven itinerant magnetism in altermagnets, Phys. Rev. B **111**, L020401 (2025).
[9] S. Lee, S. Lee, S. Jung, J. Jung, D. Kim, Y. Lee, B. Seok, J. Kim, B. G. Park, L. Šmejkal, C.-J. Kang, and C. Kim, Broken kramers degeneracy in altermagnetic MnTe, Physical Review Letters **132**, 036702 (2024).
[10] S. Reimers, L. Odenbreit, L. Šmejkal, V. N. Strocov, P. Constantinou, A. B. Hellenes, R. Jaeschke-Ubiergo, W. H. Campos, V. K. Bharadwaj, A. Chakraborty, T. Denneulin, W. Shi, R. E. Dunin-Borkowski, S. Das, M. Kläui, J. Sinova, and M. Jourdan, Direct observation of altermagnetic band splitting in CrSb thin films, Nature Communications **15**, 2116 (2024).
[11] B. Jiang, M. Hu, J. Bai, Z. Song, C. Mu, G. Qu, W. Li, W. Zhu, H. Pi, Z. Wei, Y. Sun, Y. Huang, X. Zheng, Y. Peng, L. He, S. Li, J. Luo, Z. Li, G. Chen, H. Li, H. Weng, and T. Qian, A metallic room-temperature *d*-wave altermagnet, Nature Physics **21**, 754 (2025).
[12] R. González-Hernández, L. Šmejkal, K. Symonova, *et al.*, Crystal time-reversal spin rotation symmetry breaking in collinear antiferromagnets, Physical Review Letters **126**, 127701 (2021).
[13] Z. Feng *et al.*, Spin splitting and spin current in altermagnetic materials, Nature Communications **13**, 4258 (2022).
[14] T. Jungwirth, L. Šmejkal, J. Sinova, R. González-Hernández, *et al.*, Altermagnetic spintronics, arXiv preprint https://doi.org/10.48550/arXiv.2508.09748 (2025), arXiv:2508.09748, 2508.09748.
[15] L.-D. Yuan, Z. Wang, J.-W. Luo, E. I. Rashba, and A. Zunger, Giant momentum-dependent spin splitting in centrosymmetric low-*z* antiferromagnets, Physical Review B **102**, 014422 (2020).
[16] J. Sødequist and T. Olsen, Two-dimensional altermagnets from high-throughput computational screening:

Symmetry requirements, chiral magnons, and spin-orbit effects, Applied Physics Letters **124**, 182409 (2024).
[17] T. Jungwirth, J. Sinova, R. M. Fernandes, Q. Liu, H. Watanabe, S. Murakami, S. Nakatsuji, and L. Šmejkal, Symmetry, microscopy and spectroscopy signatures of altermagnetism, Nature **649**, 837 (2026).
[18] R. Bhattarai, P. Minch, and T. D. Rhone, High-throughput screening of altermagnetic materials, Physical Review Materials **9**, 064403 (2025).
[19] L. Bai, W. Feng, S. Liu, L. Šmejkal, Y. Mokrousov, and Y. Yao, Altermagnetism: Exploring new frontiers in magnetism and spintronics, Advanced Functional Materials **34**, 2409327 (2024).
[20] R. Tamang, S. Gurung, D. P. Rai, S. Brahimi, and S. Lounis, Altermagnetism and altermagnets: A brief review, Magnetism **5**, 17 (2025).
[21] P. A. McClarty and J. G. Rau, Landau theory of altermagnetism, Physical Review Letters **132**, 176702 (2024).
[22] Q. Song, S. Stavrić, P. Barone, A. Droghetti, D. S. Antonenko, J. W. F. Venderbos, C. A. Occhialini, B. Ilyas, E. Ergeçen, N. Gedik, *et al.*, Electrical switching of a *p*-wave magnet, Nature **642**, 64 (2025).
[23] S. Brahimi, D. Prakash Rai, and S. Lounis, Confinement-induced altermagnetism in RuO_2 ultrathin films, J. of Phys.: Condens. Matter **37**, 395801 (2025).
[24] Y. Fukaya, B. Lu, K. Yada, Y. Tanaka, and J. Cayao, Superconducting phenomena in systems with unconventional magnets, Journal of Physics: Condensed Matter **37**, 313003 (2025).
[25] R. Saito, G. Dresselhaus, and M. S. Dresselhaus, *Physical Properties of Carbon Nanotubes* (Imperial College Press, London, 1998).
[26] M. S. Dresselhaus, G. Dresselhaus, and P. Avouris, *Carbon Nanotubes: Synthesis, Structure, Properties, and Applications* (Springer, Berlin, 2001).
[27] Y. Nakanishi *et al.*, Structural diversity of single-walled transition metal dichalcogenide nanotubes grown via template reaction, Advanced Materials **35**, 2306631 (2023).
[28] M. Liu *et al.*, Photoluminescence from single-walled MoS_2 nanotubes coaxially grown on boron nitride nanotubes, ACS Nano **15**, 8418 (2021).
[29] W. Dai *et al.*, Metallic NbS_2 one-dimensional van der waals heterostructures, ACS Nano **19**, 32800 (2025).
[30] C. Yang *et al.*, Janus MoSSe nanotubes on 1d swcnt-bnnt van der waals heterostructures, Small **21**, 2570208 (2025).
[31] A. E. Mikkelsen, F. T. Bölle, K. S. Thygesen, T. Vegge, and I. E. Castelli, Band structure of MoSTe janus nanotubes, Physical Review Materials **5**, 014002 (2021).
[32] S. Zhao, C. Yang, Z. Zhu, X. Yao, and W. Li, Curvature-controlled band alignment transition in 1d van der waals heterostructures, npj Computational Materials **9**, 92 (2023).
[33] A. Ablimit, Y.-J. Sun, H. Jiang, C. Wu, L. Wei, X. Chen, and G. Cao, Weak metal–metal transition in the vanadium oxytelluride $Rb_{1-\delta}V_2Te_2O$, Physical Review Materials **2**, 044801 (2018).
[34] X. Cheng, Y. Gao, J. Peng, and J. Liu, Realistic tight-binding model for V_2Se_2O-family altermagnets, arXiv (2026), arXiv:2602.09465 [cond-mat.mtrl-sci].
[35] R. Xu, Y. Gao, and J. Liu, Chemical design of monolayer altermagnets, National Science Review **13**, nwaf528 (2026).
[36] A. González-García, W. López-Pérez, P. Pacheco, L. Ramírez-Montes, and R. González-Hernández, Coexistence of d-wave altermagnetism and topological states in janus FeSe X (X= S, Te) monolayers, Physical Review Materials **10**, 044004 (2026).
[37] W.-H. Kang, Y.-T. Hsiao, J. Genzor, Y. Zhumagulov, M.-H. Liu, and D. Kochan, Efficient Magnetic Spin-Filtering and Persistent Spin-Currents in Lifshitz-Transitioned Altermagnets: A Route to Open-Orbit Spintronics, arXiv preprint arXiv:2606.04587 (2026), arXiv:2606.04587 [cond-mat.mes-hall].
[38] Z. Jin, R. R. Neumann, R. Jaeschke-Ubiergo, J. Sinova, and A. Mook, Rolling two-dimensional collinear magnets into chiral nanotubes with *p*-wave magnetism, arXiv preprint arXiv:2606.30214 (2026), arXiv:2606.30214 [cond-mat.mes-hall].
[39] S. Smidstrup, T. Markussen, P. Vancraeyveld, J. Wellendorff, J. Schneider, T. Gunst, B. Verstichel, D. Stradi, P. A. Khomyakov, U. G. Vej-Hansen, M.-E. Lee, S. T. Chill, F. Rasmussen, G. Penazzi, F. Corsetti, A. Ojanperä, K. Jensen, M. L. N. Palsgaard, U. Martinez, A. Blom, M. Brandbyge, and K. Stokbro, QuantumATK: an integrated platform of electronic and atomic-scale modelling tools, J. Phys.: Condens. Matter **32**, 015901 (2019).
[40] J. P. Perdew, K. Burke, and M. Ernzerhof, Generalized gradient approximation made simple, Phys. Rev. Lett. **77**, 3865 (1996).
[41] M. J. Van Setten, M. Giantomassi, E. Bousquet, M. J. Verstraete, D. R. Hamann, X. Gonze, and G.-M. Rignanese, The PseudoDojo: Training and grading a 85 element optimized norm-conserving pseudopotential table, Comput. Phys. Commun. **226**, 39 (2018).

Supplementary Files

This is a list of supplementary files associated with this preprint. Click to download.

- SINanotubes.pdf